Supplementary Information

Fluorine-rich Modification of Self-Extinguishable Lithium-Ion Battery Separators using Cross-linking Networks of Chemically Functionalized PVDF Terpolymers for Highly Enhanced Electrolyte Affinity and Thermal, Mechanical Stability

Jaewon Park[a,‡], Young Je Kwon[a,‡], Jeongsik Yun[b,‡], Ji Woo Bae [a], Min Jeong Lee [a], Kaiyun Zhang [a], Se Hun Kim[a], Kang-Jun Baeg[c], Jin Hong Lee[d], Kie Yong Cho[a,*]

[a] Department of Industrial Chemistry, Pukyong National University, 45 Yongso-Ro, Nam-Gu, Busan 48513, Republic of Korea.

[b] Department of Energy and Chemical Engineering, Incheon National University, 119 Academy-ro, Yeonsu-gu, Incheon 22012, Republic of Korea

[c] Department of Nanotechnology Engineering, Pukyong National University, 45, Yongso-ro, Nam-gu, Busan, 48513 Republic of Korea

[d] School of Chemical Engineering, Pusan National University, Busan 46421, Republic of Korea.

[‡]These authors contributed equally to this work

*Corresponding author e-mail: kieyongh@pknu.ac.kr (K. Y. Cho)

Keywords: separators, crosslinkable PVDF, dip-coating process, self-extinguish, Li-ion batteries

Supplementary Information

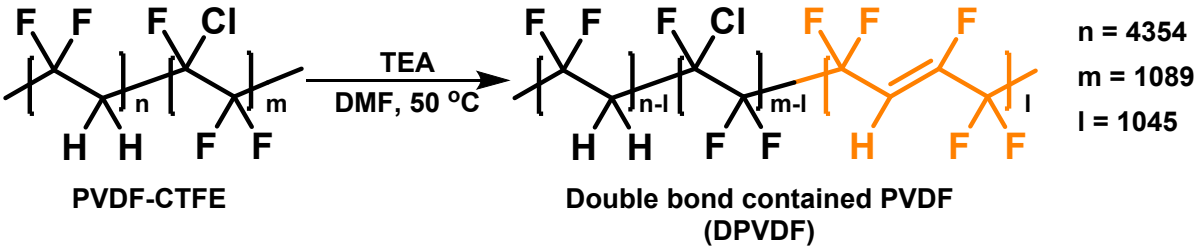

Fig. S1. A scheme for synthesizing double bond-contained PVDF (DPVDF). The repeating numbers for each monomer were calculated using ^{1}H NMR, GPC data for PVDF-CTFE and DPVDF.

Supplementary Information

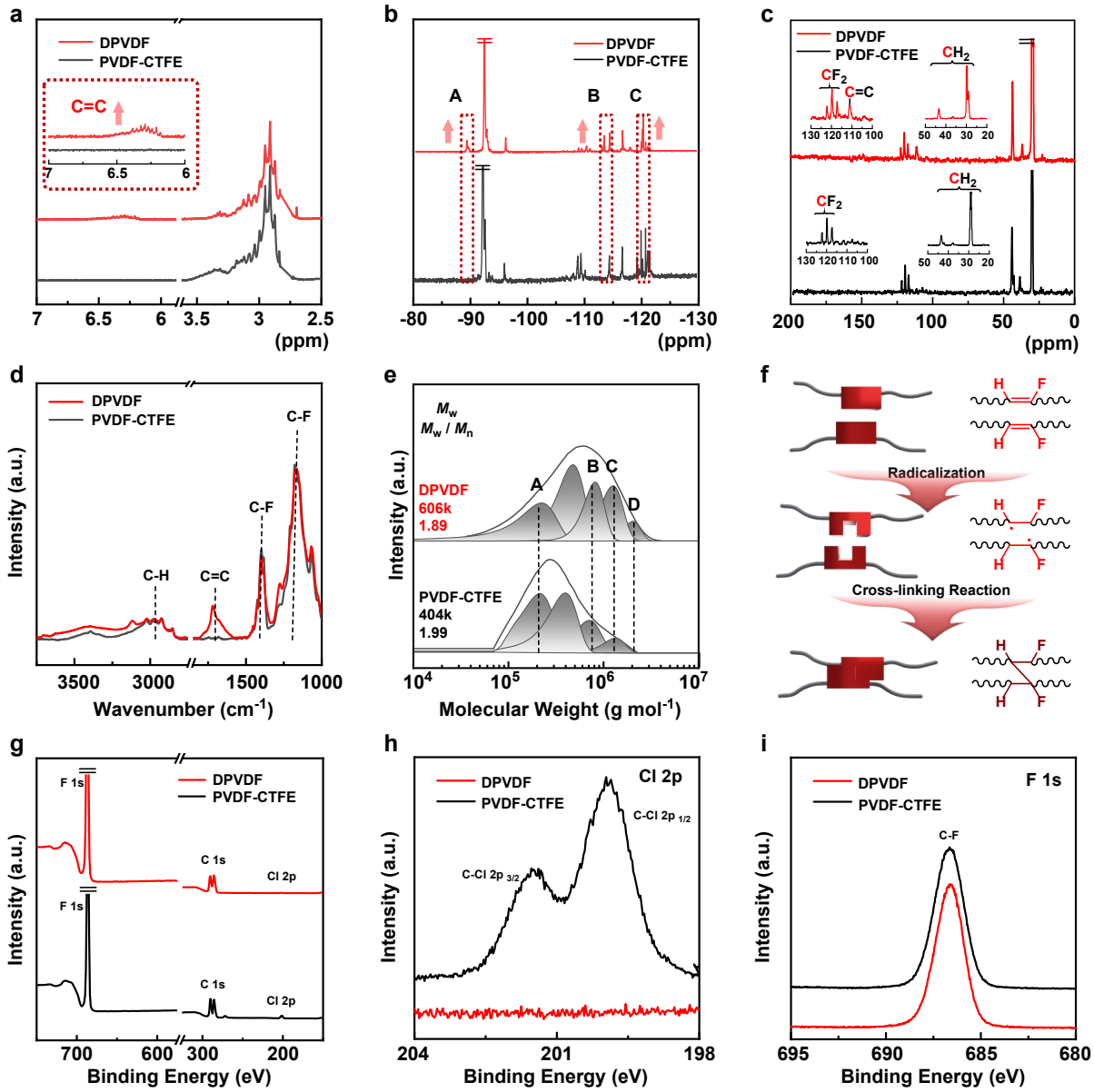

Fig. S2. a) ^{1}H NMR, b) ^{19}F NMR, and c) ^{13}C NMR spectra of PVDF-CTFE and DPVDF in Acetone-d_6. d) FT-IR spectra of PVDF-CTFE and DPVDF. e) Gel permeation chromatography (GPC) curves for PVDF-CTFE and DPVDF with deconvolution for molecular weight distribution. f) Schematic illustration of the cross-linking reaction for DPVDF. g) XPS survey spectra of DPVDF and PVDF-CTFE. XPS narrow scan spectra of DPVDF and PVDF-CTFE for h) Cl 2p and i) F 1s.

The progress of the dehydrochlorination reaction was tracked using ^{1}H NMR, which revealed a 96% conversion of CTFE to DPVDF with double bonds integrated at 19.9 mol% in DPVDF (Fig. S2a). The presence of double bond groups (-CF_2-CF=CH-CF_2-) in the DPVDF backbone was confirmed by ^{1}H NMR, which yielded a new peak at 6.3 ppm (Fig. S2a). The successful introduction of double bonds into PVDF-CTFE was further verified by ^{19}F NMR,

which showed double bond sequence peaks of (see dashed-squares in Fig. S2b) (A) –$CF{=}CHCF_2CH_2CF_2$– (-89.3 ppm), (B) –$CF_2CF_2CF{=}CHCF_2$–, –$CF_2CH_2CF_2CF_2CF{=}CH$– (-113.4 and -113.8 ppm), and (C) –$CH_2CF_2CF{\neg}CF{=}CH$– (-120.4 ppm) (Fig. S2b). The introduction of double bonds was also verified with ^{13}C NMR. As seen in Fig. S2c, double bond peaks are observed at 112 ppm in ^{13}C NMR. Moreover, the presence of a strong -C=C- stretching peak at 1,720 cm^{-1} in the FT-IR spectra confirmed the functionalization of double bonds in DPVDF (Fig. S2d). Additionally, molecular weight measurements were performed using GPC, demonstrating an increase in molecular weight of PVDF-CTFE from 404,000 g mol^{-1} to 606,000 g mol^{-1} (DPVDF), as shown in Figure S2e.

The molecular weight of PVDF-CTFE and the prepared DPVDF is analyzed with the GPC using DMF eluent with PMMA standard. The molecular weights of PVDF-CTFE and DPVDF demonstrate an increase in molecular weight from 404,000 g mol^{-1} to 606,000 g mol^{-1}, as shown in Fig. S2e. The deconvolution of GPC curves for PVDF-CTFE and DPVDF shows that the peak intensity for lower molecular weight (A) and higher molecular weight region (B and C) changed. In other words, the lower molecular weight region of DPVDF (A) decreased, and the higher molecular weight region of DPVDF (B and C) increased relative to PVDF-CTFE. In addition, the several cross-linking reactions of DPVDF led to the new peak at D. The increase in molecular weight is attributed to cross-linking reactions, which occur due to the generation of radical species during the DPVDF synthesis. Fig. S2f illustrates the reaction mechanism: π-bond in double bonds can be dissociated and then generated radical active sites. The generated radicals can initiate cross-linking reactions with other double bonds during the dehydrochlorination reaction. In turn, molecular weight increased by the radical species-induced cross-linking reaction (Fig. S2f).

To identify the mechanism of double bonding generations, FT-IR analysis of DPVDF and PVDF-CTFE were performed under identical measurement conditions (the same thickness); because double bonds can be made either by dehydrofluorination of PVDF or dehydrochlorination of CTFE. As can be seen in Fig. S2d, the C-H and C-F peaks show negligible alterations, while strong evidence for the C=C formation is confirmed, which indicates that C-F is not consumed in the generation of C=C. Furthermore, XPS analysis was conducted to identify the presence of Cl and F in PVDF-CTFE and DPVDF. We examined the atomic composition of C, F, and Cl through XPS (Fig. S2g). In PVDF-CTFE, the atomic proportions were C: 63.2%, F: 35.8%, and Cl: 1.0%, while PVDF-CTFE exhibits the atomic

proportions of C: 64.4%, F: 35.5%, and Cl: 0.1%. In contrast to the very similar values of C and F in both PVDF-CTFE and DPVDF, a significant decrease was observed in the Cl proportion. In both polymers, the F 1s peaks were clearly visible (Fig. S2h). In strong contrast, the Cl 2p peaks in PVDF-CTFE are clearly evident, while Cl 2p peaks are absent in DPVDF. Therefore, it is confirmed that dehydrofluorination reactions do not occur during the synthesis (Fig. S2i). Moreover, Tan *et al.* reported that neat PVDF does not react with triethylamine (TEA) under mild conditions, but the reaction occurs at a high temperature of 80 ^{o}C.[1] ^{1}H NMR analysis of the PVDF that reacted with TEA did not show double bond peaks between 6.0 and 6.5 ppm, showing the inactivity of the dehydrofluorination reactions. Note that the synthesis of DPVDF was conducted at 50 ^{o}C.

Supplementary Information

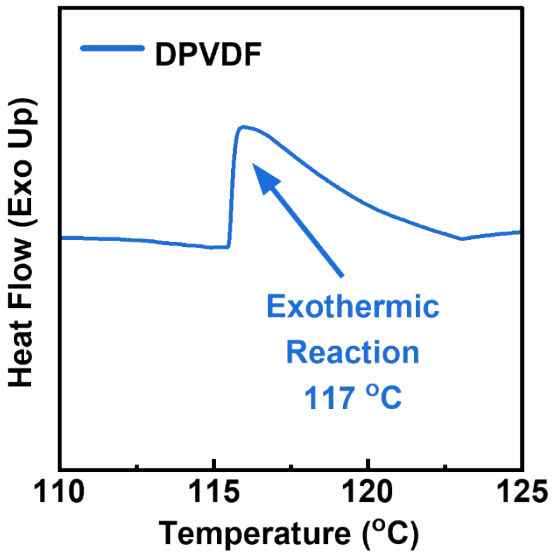

Fig. S3. 1st run DSC curve of DPVDF at the temperatures ranging from 50 to 200 °C with a heating rate of 5 °C min^{-1} under N_2.

Supplementary Information

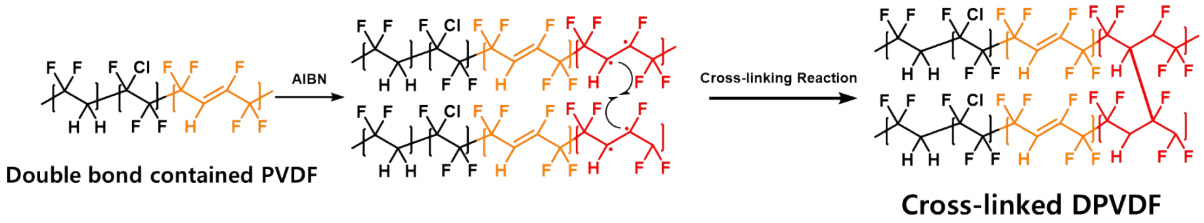

Fig. S4. A Scheme for cross-linking reaction of DPVDF

Supplementary Information

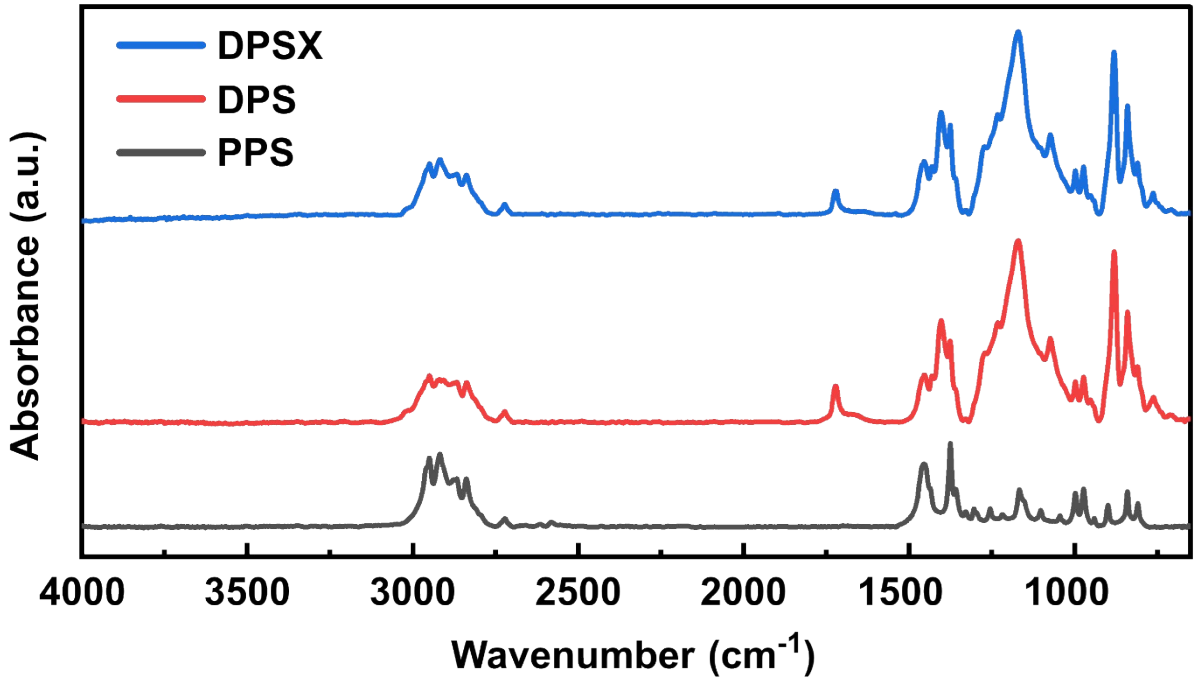

Fig. S5. FT-IR spectra of PPS, DPS, and DPSX separators.

Supplementary Information

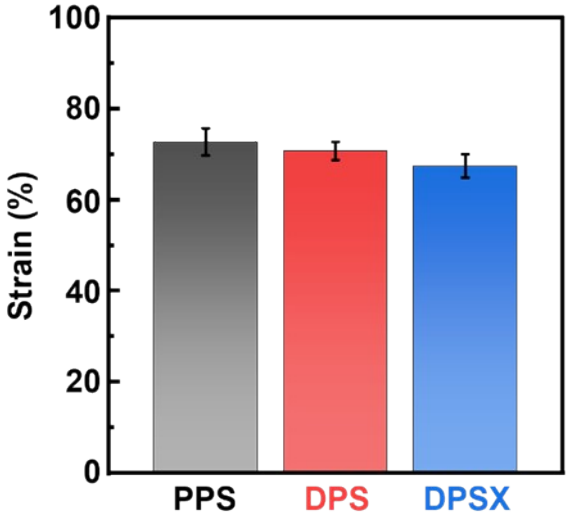

Fig. S6. Tensile strain of PPS, DPS, and DPSX.

Supplementary Information

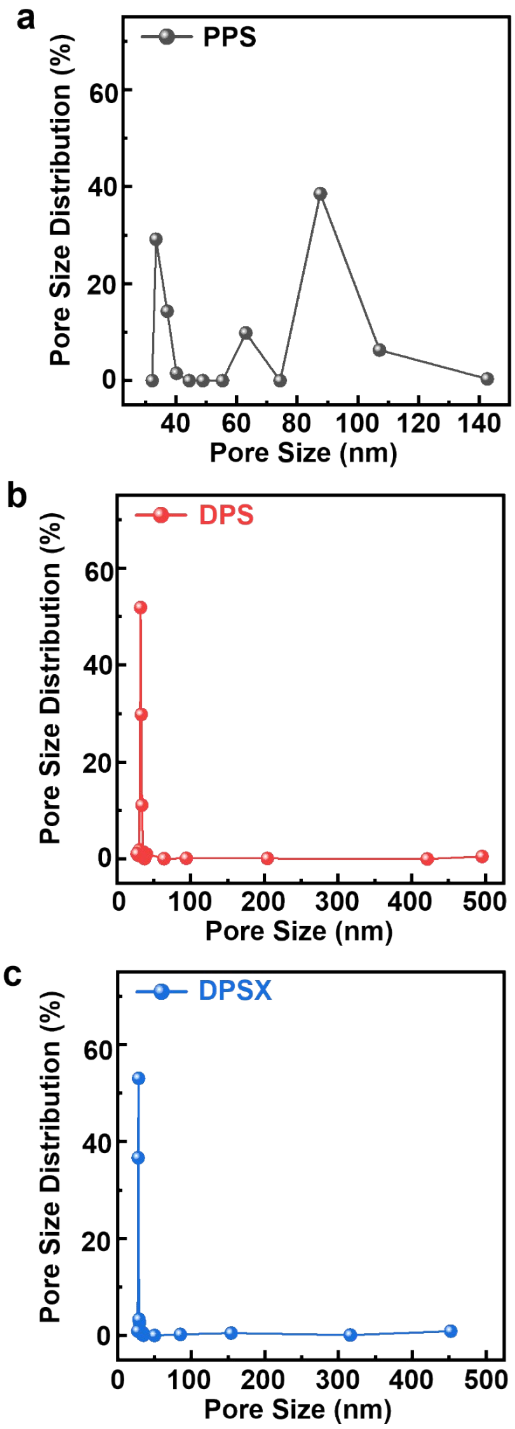

Fig. S7. Full spectra of the pore size distribution of a) PP separator, b) DPS, and c) DPSX.

Supplementary Information

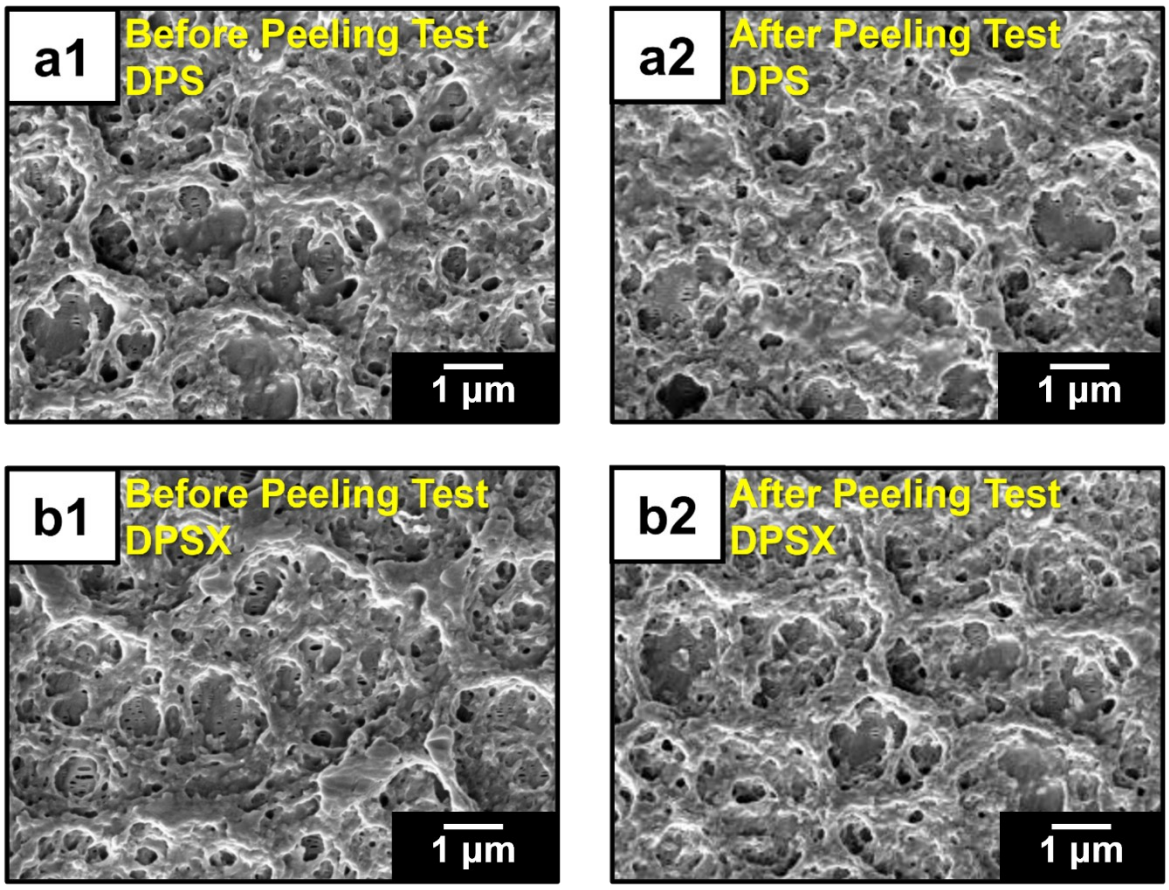

Fig. S8. SEM Images of DPS and DPSX before and after peeling off tests

Supplementary Information

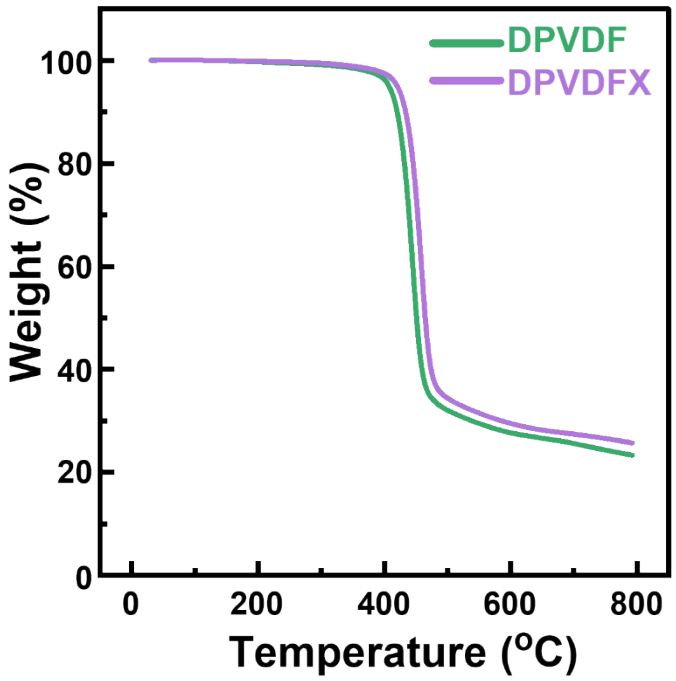

Fig. S9. TGA curves of DPVDF and cross-linked DPVDF (DPVDFX) with heating rate of 10 $^{o}C\ min^{-1}$ under N_2.

Supplementary Information

	PPS	DPS[1]	DPSX[2]	DPVDF	DPVDFX
T_d 1% (°C)	286.07	394.07	411.47	395.55	415.35
Residue (%)	0.17	2.88	3.31	23.31	25.68

Table S1. TGA profiles of PP separator, DPVDF, DPVDFX, DPS and DPSX.

[1,2] DPVDF coating weight per unit area is ca. 18.144g m^{-2}

Supplementary Information

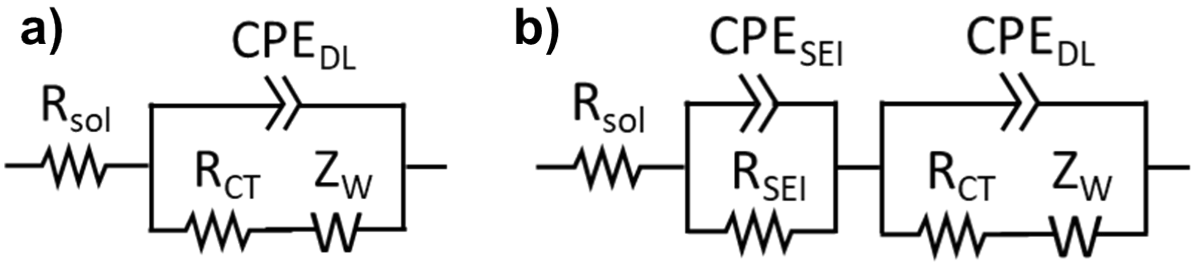

Fig. S10. Equivalent circuit model (EEC) for EIS fitting impedance spectra: a) simple Randels circuit including Warburg element (diffusion) and b) EEC model with consideration of solid-electrolyte-interphase (SEI) layers.

Supplementary Information

Table S2. EIS fitting results for LFP half cells with PPS, DPS, and DPSX. R_{sol}: solution resistance, R_{SEI}: resistance for solid-electrolyte-interphase (SEI), Q_{SEI}, n_{SEI}: characteristic parameters of constant phase element (CPE) describing a SEI layer, R_{CT}: charge-transfer resistance, Q_{DL}, n_{DL}: characteristic parameters of CPE describing electrochemical double layer, and W: Warburg impedance.

	Separator	R_{sol} (Ohm)	R_{SEI} (Ohm)	Q_{SEI}	n_{SEI}	R_{CT} (Ohm)	Q_{DL} (Ohm)	n_{DL}	W (Ohm)
Before	**PPS**	1.27	n/a	n/a	n/a	461.81	1.60E-05	0.69378	232.59
	DPS	1.57	n/a	n/a	n/a	429.62	2.77E-05	0.63281	283.51
	DPSX	2.12	n/a	n/a	n/a	366.47	2.57E-05	0.67967	145.92
After	**PPS**	6.6785	5.7794	750.46	2.30E-06	0.87173	1.17E-05	8.51E-01	37.256
	DPS	6.664	7.544	644	6.91E-05	0.60491	1.15E-05	0.90082	26.834
	DPSX	6.9178	6.031	592.74	8.78E+01	4.67E-06	9.14E-06	0.87678	0.80846

Supplementary Information

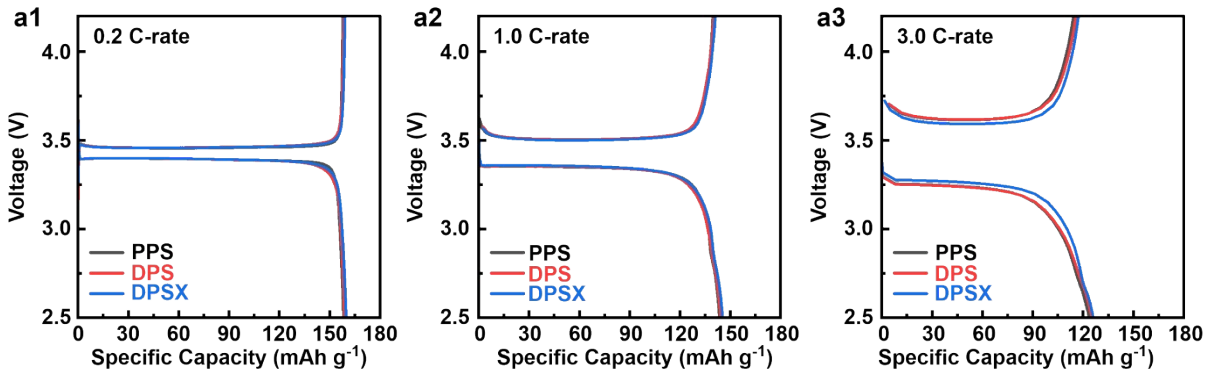

Fig. S11. Charge-discharge voltage profiles of LFP half cells (LFP | separator | Li-metal) with PPS (black), DPS (red), and DPSX (blue) at different C-rate a1) 0.2 C, a2) 1.0 C, and a3) 3.0 C.

Supplementary Information

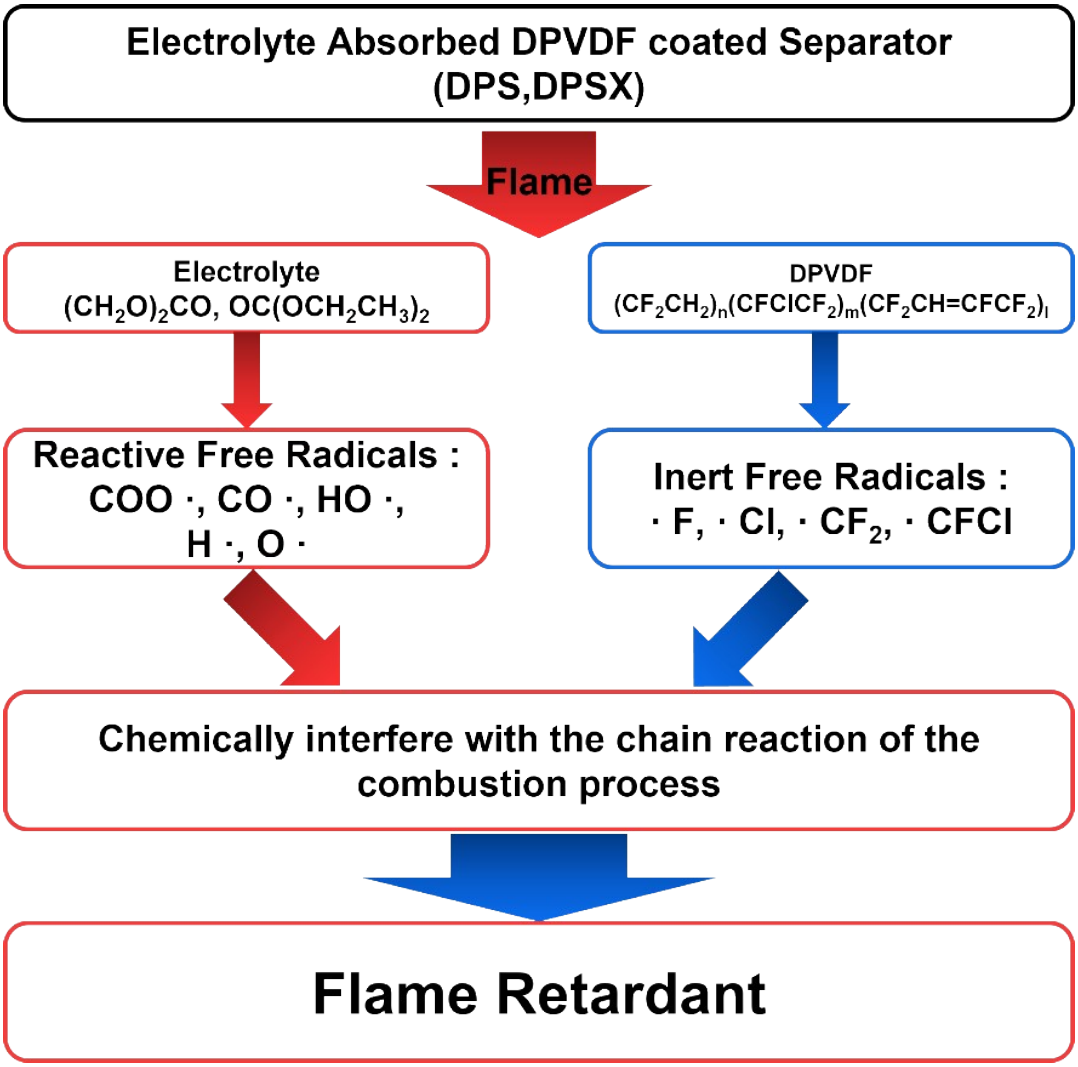

Fig. S12. A plausible diagram of the extinguishing mechanism of DPVDF-modified separators.

Supplementary Information

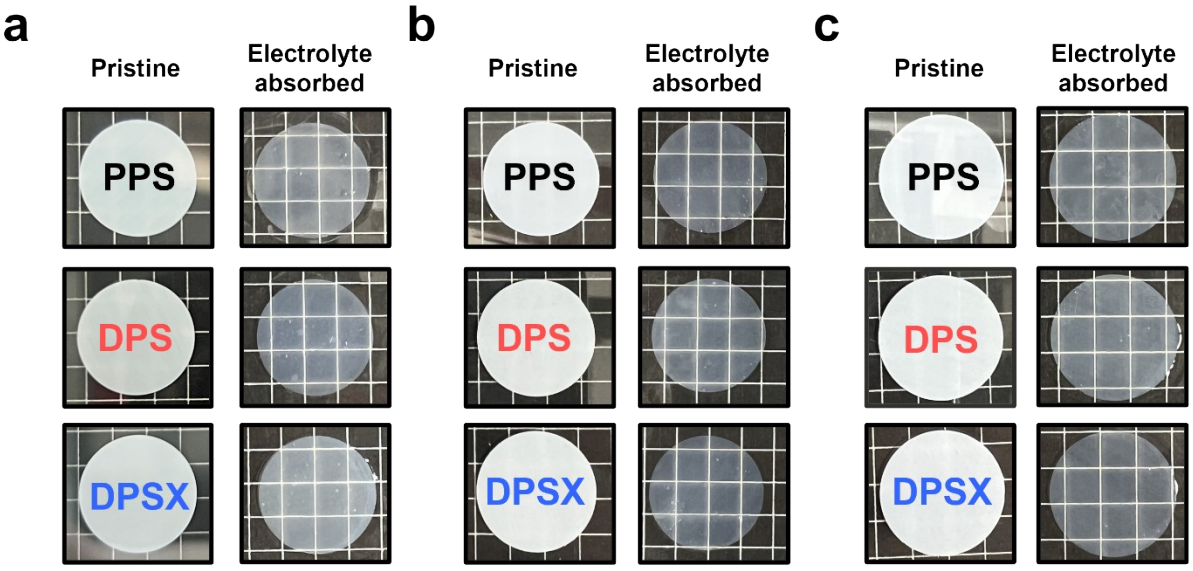

Fig. S13 Photographs of dimensional stability test of PPS, DPS and DPSX in different electrolytes. Left) pristine- and right) electrolyte-absorbed PPS, DPS, and DPSX. a) 1 M LiPF6 in EC:DEC (v:v = 1:1) b) 1 M LiPF6 in EC:DMC (v:v = 1:1), and c) 1 M LiTFSI in DOL:DME (v:v = 1:1).

Supplementary Information

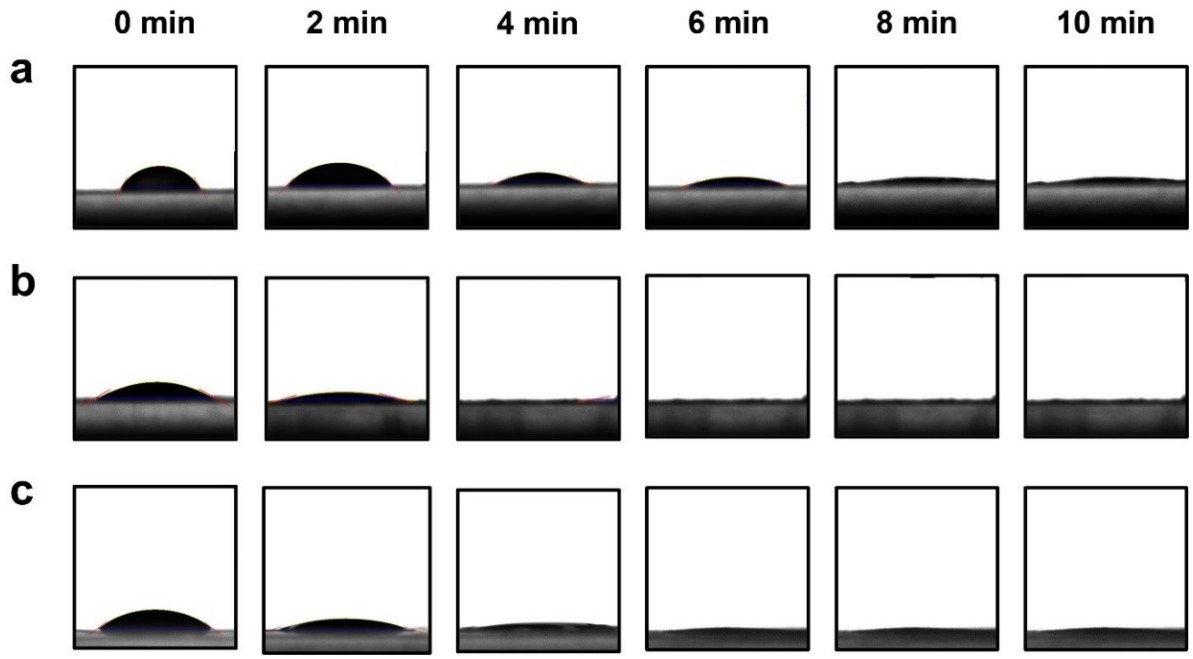

Fig. S14. Contact angle images of a) PPS, b) DPS, and c) DPSX over time using 1M LiPF6 in EC:DEC (1:1, v:v) electrolyte.

The contact angle evolution of PPS, DPS and DPSX are investigated using 1M $LiPF_6$ in EC:DEC (1:1, v:v) electrolyte. As shown in **Fig. S14**, flat surfaces are observed at DPS DPSX after 4min, showing complete wetting, whereas PPS is not fully wetted even after 10 min.

Supplementary Information

References

1 S. Tan, J. Li, G. Gao, H. Li and Z. Zhang, *J. Mater. Chem.*, 2012, **22**, 18496-18504.

2 D. Ponnamma, J. George, M. G. Thomas, C. H. Chan, S. Valić, M. Mozetič, U. Cvelbar and S. Thomas, *Polym. Eng. Sci.*, 2015, **55**, 1203-1210.